nature nanotechnology

Article

https://doi.org/10.1038/s41565-023-01497-x

Low Ohmic contact resistance and high on/off ratio in transition metal dichalcogenides field-effect transistors via residue-free transfer

In the format provided by the authors and unedited

Supplementary Information:

Table of Contents:

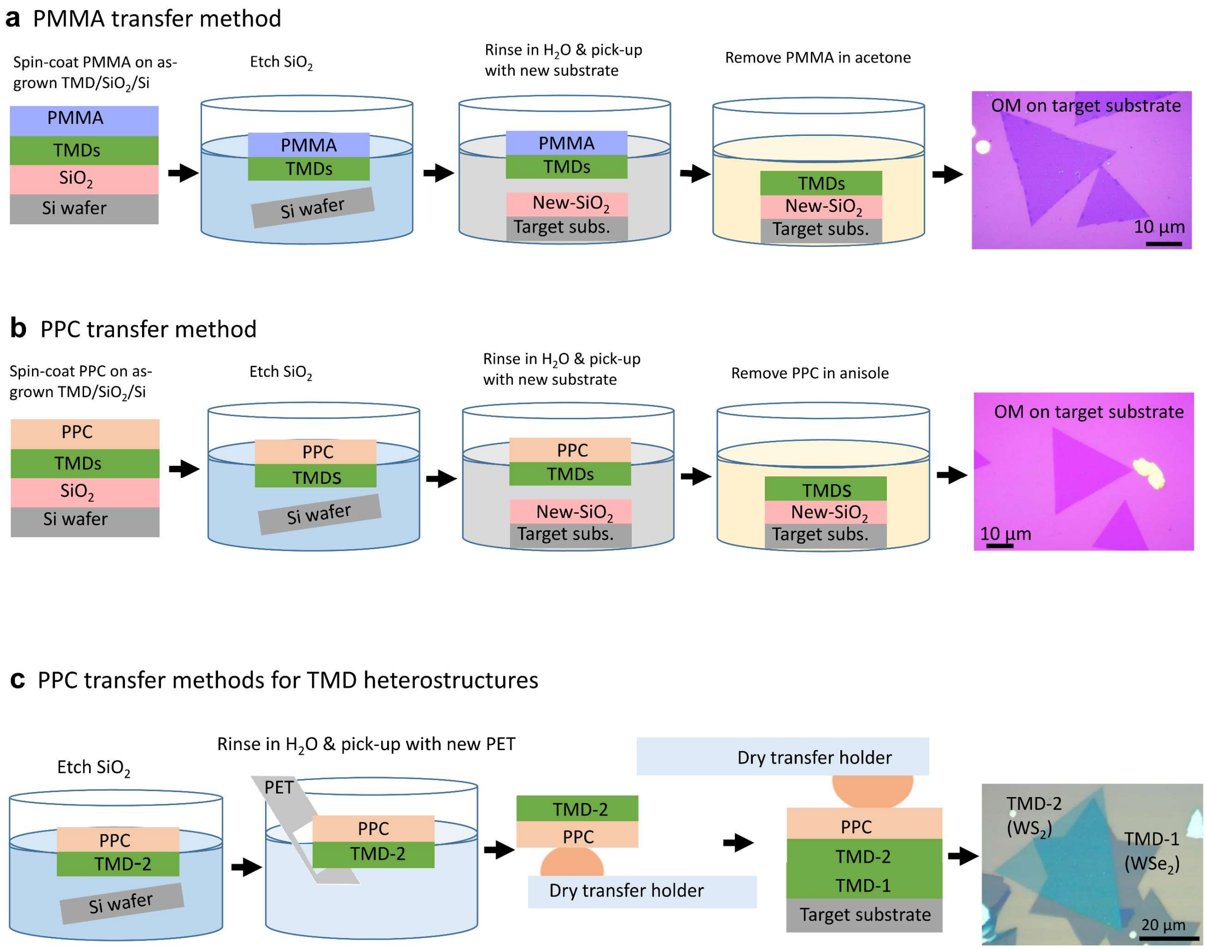

Supplementary Fig. 1 | PMMA, PPC transfer methods for monolayer TMD and heterostructure. a, Conventional PMMA wet-transfer method for monolayer TMDs. **b**, Residue-free PPC transfer method implemented for monolayer TMDs. **c,** TMD heterostructure reconstruction to facilitate residue-free interfacial contact using PPC.

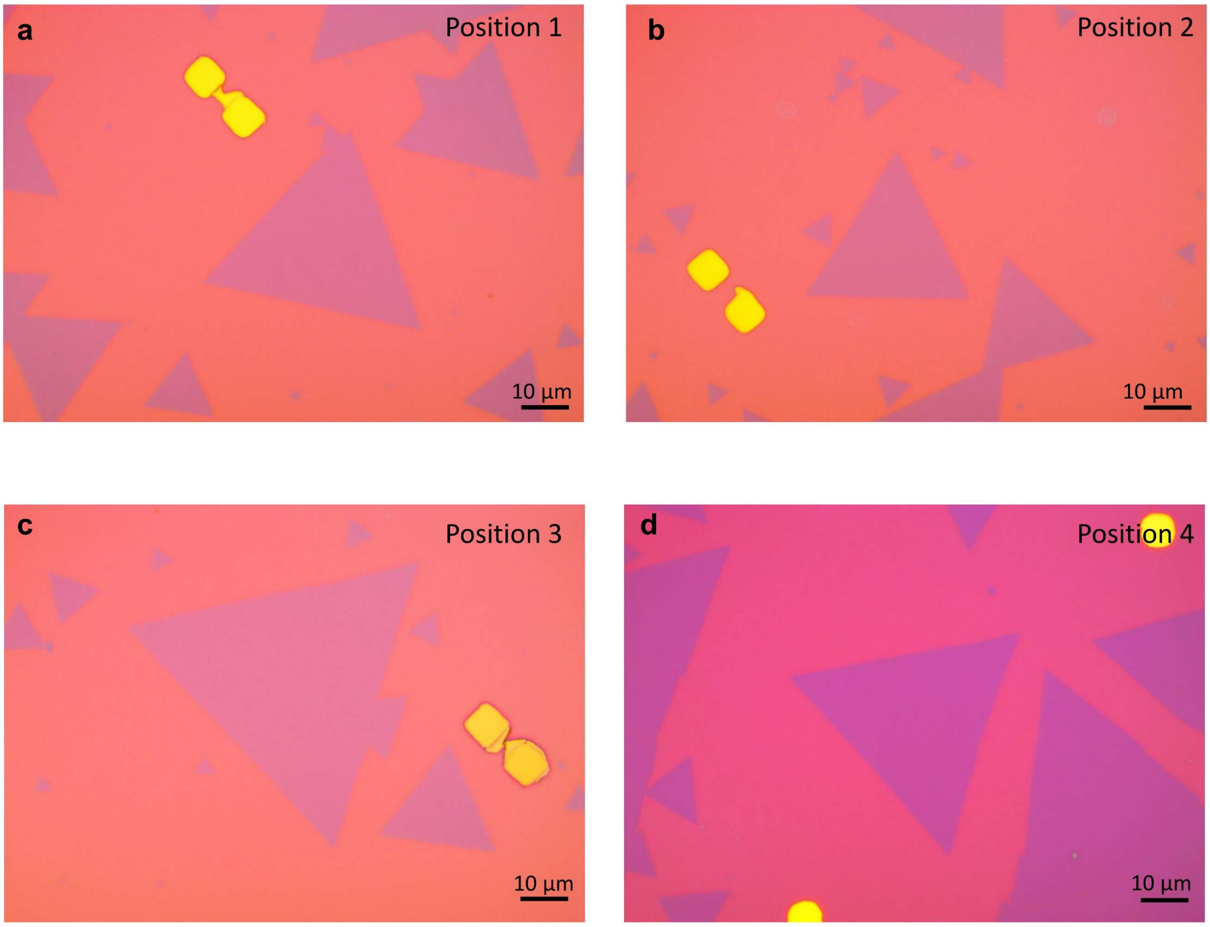

Supplementary Fig. 2 | Optical micrographs of monolayer MoS_2 (PPC method) at different positions on the substrate. a,b,c,d Optical micrographs of the PPC method at different positions on the SiO_2/Si substrate (position 1: **a**, position 2: **b**, position 3: **c**, position 4: **d**). Negligible PPC residue was observed throughout the entire substrate.

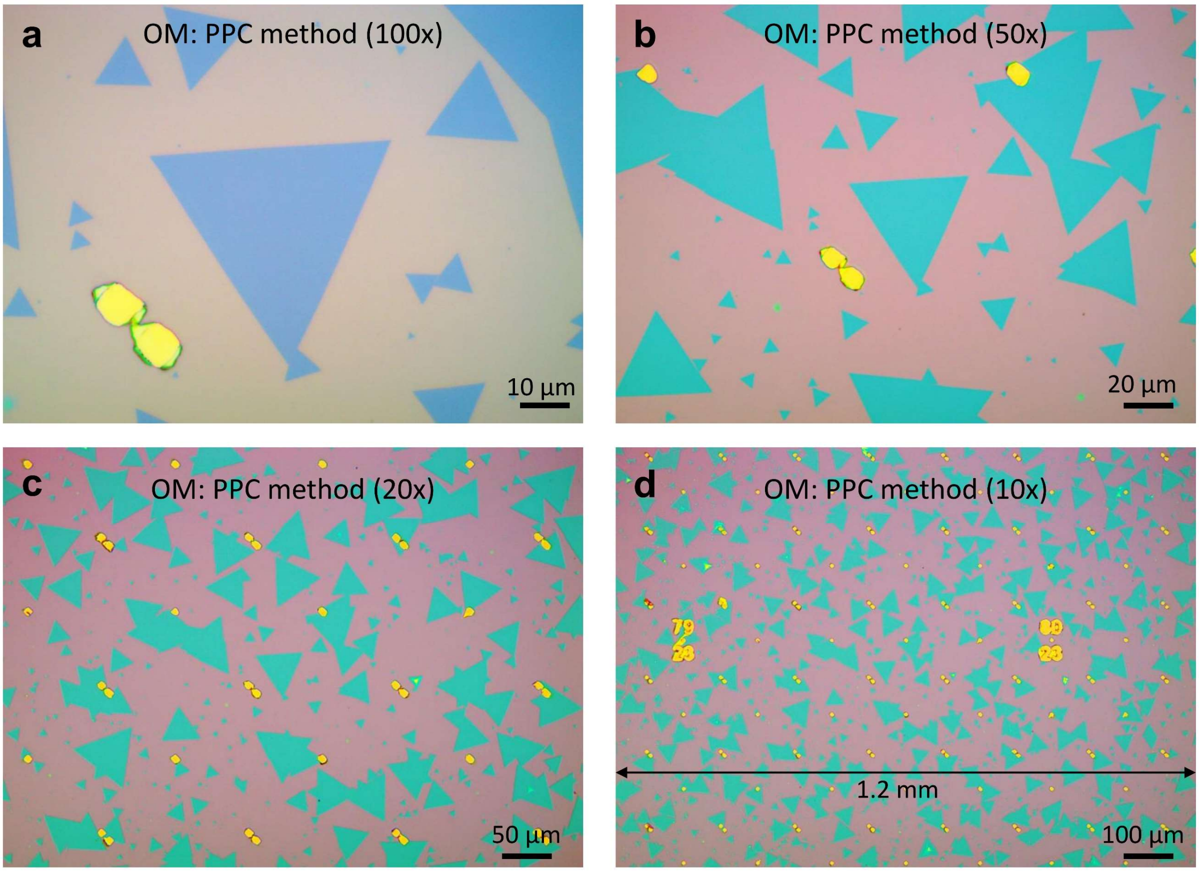

Supplementary Fig. 3 | Large-area transfer of CVD-grown MoS_2 using PPC method. a,b,c,d Optical micrographs of the monolayer MoS_2 transferred using PPC at different magnifications on the SiO_2/Si substrate.

OM comparisons using as-grown MoS_2 and MoS_2 transferred by PMMA and PPC methods

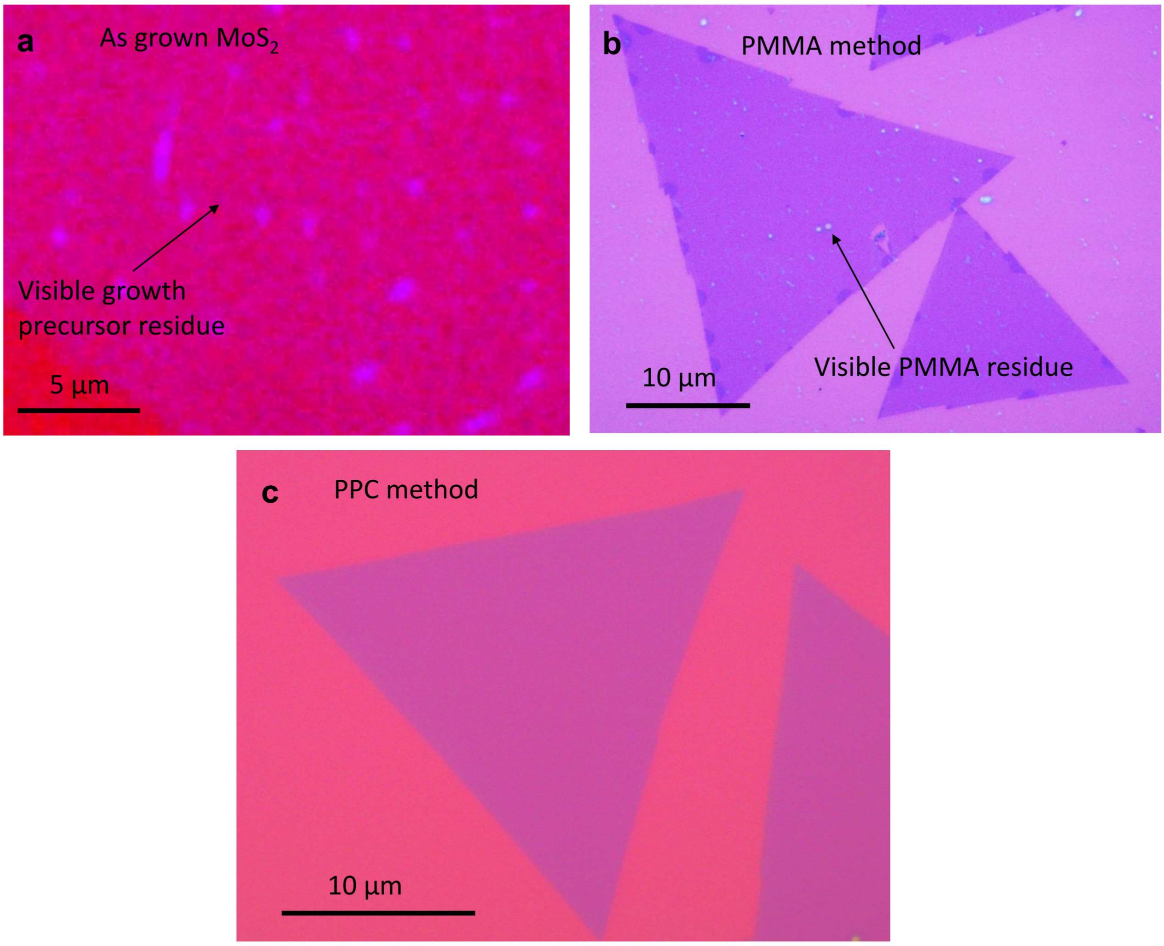

Supplementary Fig. 4 | Optical micrographs of as-grown, PMMA-transferred, PPC-transferred monolayer MoS_2. a, Optical micrograph of the as-grown monolayer MoS_2 on the growth substrate. Precursor residue spots are clearly visible on the MoS_2 surface. **b,** Optical micrograph of the monolayer MoS_2 transferred using PMMA method on the target substrate (300 nm thick SiO_2/Si). PMMA residues are often observed on the MoS_2 surface. **c,** Optical micrograph of the monolayer MoS_2 transferred using PPC method on an identical SiO_2/Si substrate. Ultraclean MoS_2 with negligible PPC residue was observed.

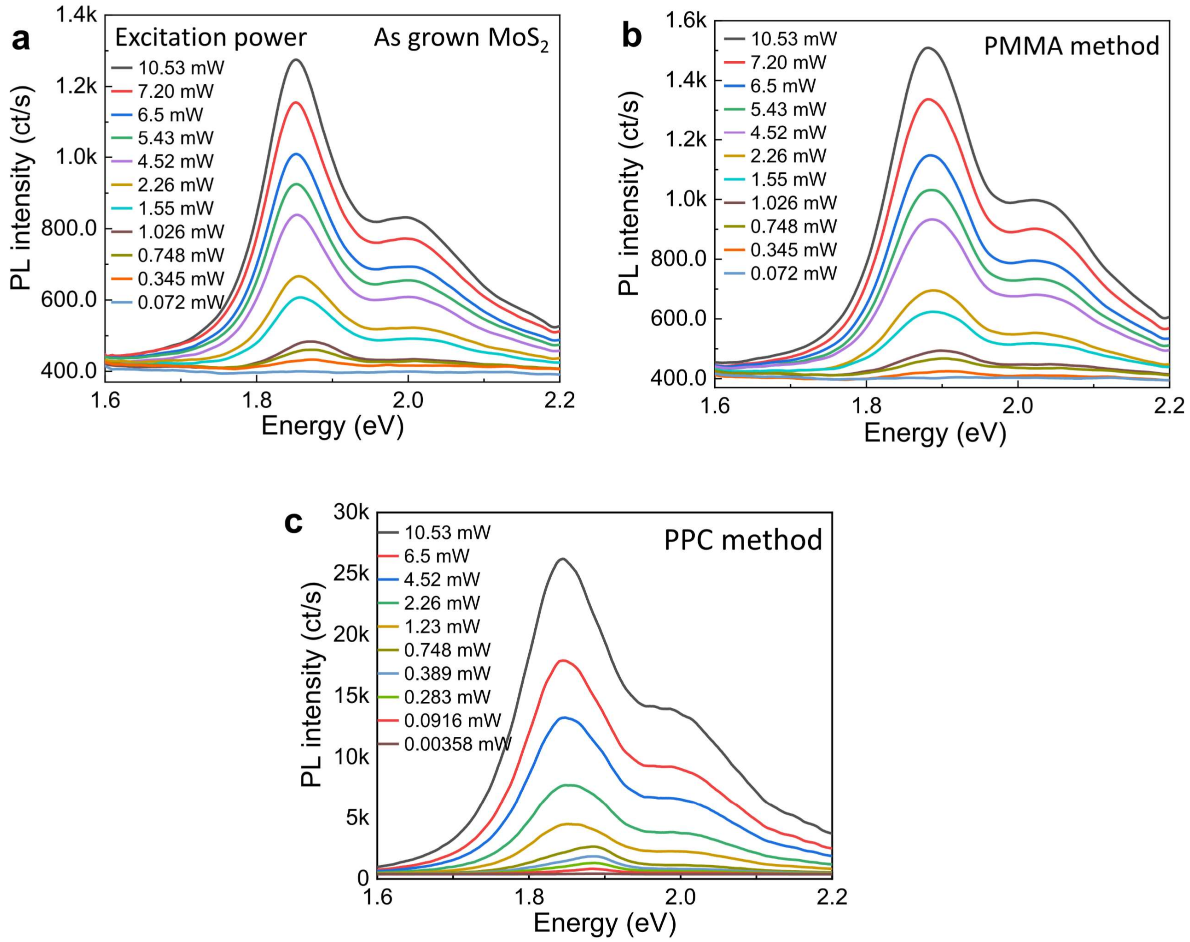

Supplementary Fig. 5 | Excitation power dependent PL comparisons of monolayer MoS_2. a,b,c, Excitation power dependent PL spectra of the monolayer MoS_2 flake for as-grown (**a**), PMMA-transferred (**b**), PPC-transferred (**c**). A laser wavelength of 532 nm was used for the PL measurement.

Device type: PPC-Bi (SiO_2/MoS_2/h-BN)

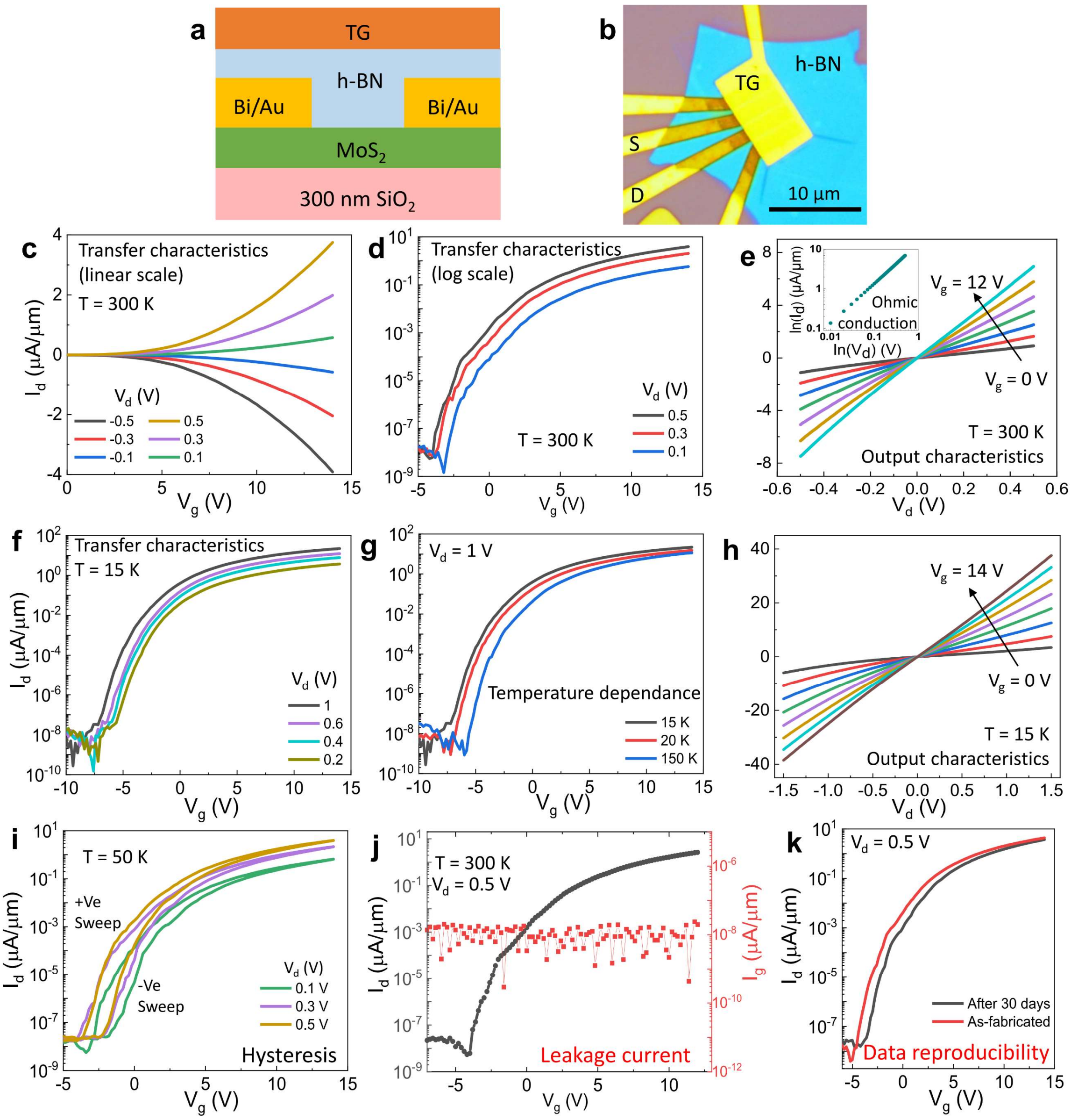

Supplementary Fig. 6 | Electrical performance of the PPC-Bi (Device2: SiO_2/MoS_2/h-BN). a,b, Schematic diagram (**a**) and optical micrograph (**b**) of the MoS_2 FET (L_{CH} = 1 μm) on SiO_2 substrate. **c,d,** Transfer characteristics (I_d-V_g) of the device plotted as a function of V_d in linear (**c**) and logarithmic (**d**) scale. **e,** Output characteristics (I_d-V_d) of the device as a function of V_g at 300 K. Inset represents the ln(I_d)-ln(V_d) plot (V_g = 12 V) that exhibits linear behavior demonstrating Ohmic conduction. **f,** I_d-V_g of the device at low temperature (15 K). **g,** Temperature-dependent I_d-V_g of the device. **h,** I_d-V_d of the device at low temperature (15 K). **i,** Measured hysteresis of the device using positive and negative gate (V_g) sweep at 50 K. **j,** Measured leakage current (I_g) of the device acquired (right red y-axis) during a typical I_d-V_g measurement (left black y-axis). **k**, Data reproducibility of the device (typical I_d-V_g plot) measured just after fabrication (as-fabricated) and after 30 days.

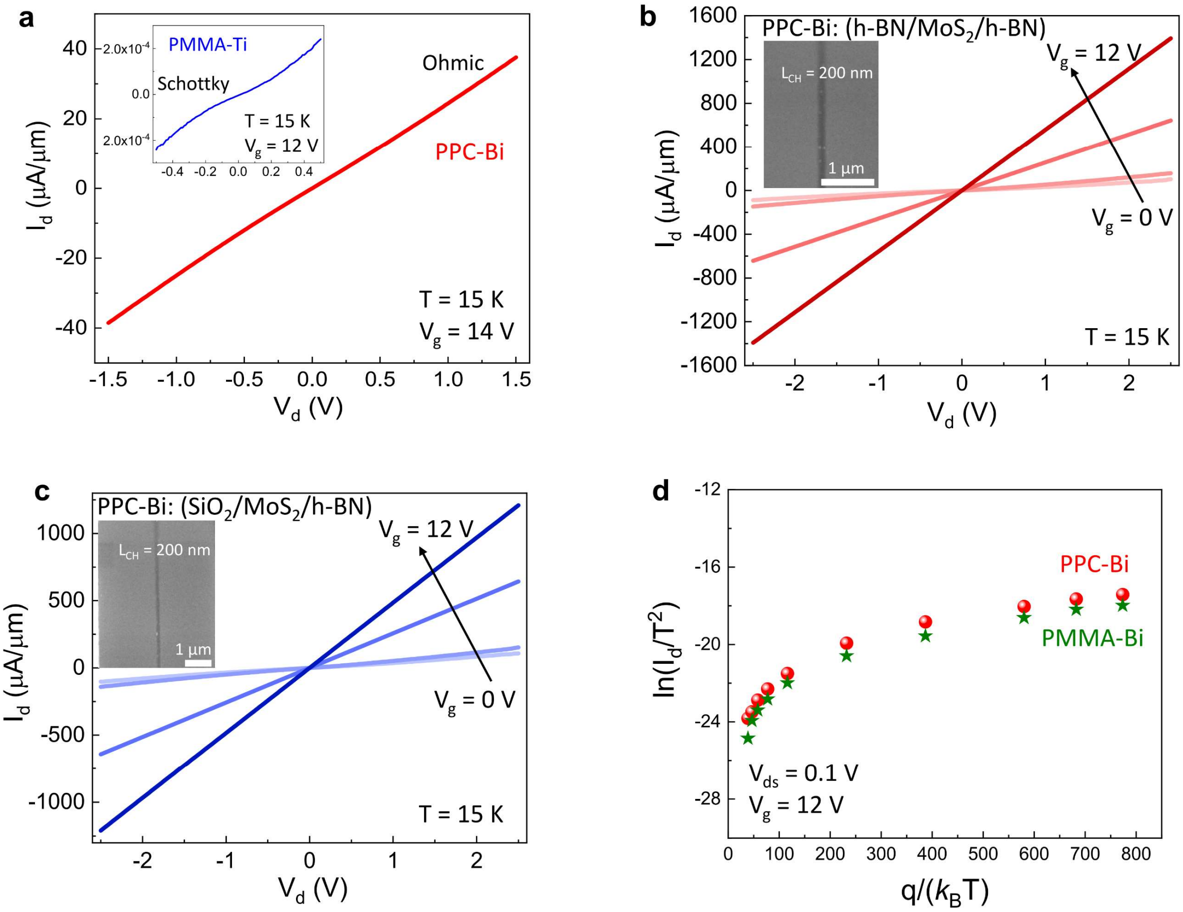

Supplementary Fig. 7 | Output characteristics comparison of different device types. a, Ohmic behavior of the PPC-Bi FET (Device2) was observed (T = 15 K, V_g = 14 V). In contrast, Schottky behavior was observed in the PMMA-Ti (Device5) FET shown in the inset at V_g = 12 V. **b,** I_d-V_d of the PPC-Bi FET on h-BN substrate (Device1: h-BN/MoS_2/h-BN) as a function of V_g at 15 K (inset shows SEM image of L_{CH} = 200 nm). High $I_{on\text{-}max} \approx 1.40$ mA/μm was achieved at 15 K. **c,** I_d-V_d of Device2 as a function of V_g at 15 K (inset shows SEM image of L_{CH} = 200 nm). **d,** I_d *vs.* T^2 plotted using thermionic emission equation $I_d = I_S\left[e^{\frac{qV}{k_BT}} - 1\right]$, where $I_S = \left[A^*T^2e^{(-\frac{q\varphi}{k_BT})}\right]$. Here A^* is the Richardson constant, q is the electric charge, k_B is the Boltzmann constant, φ is the SBH[1,2].

Device type: PPC-Bi (h-BN/MoS_2/h-BN)

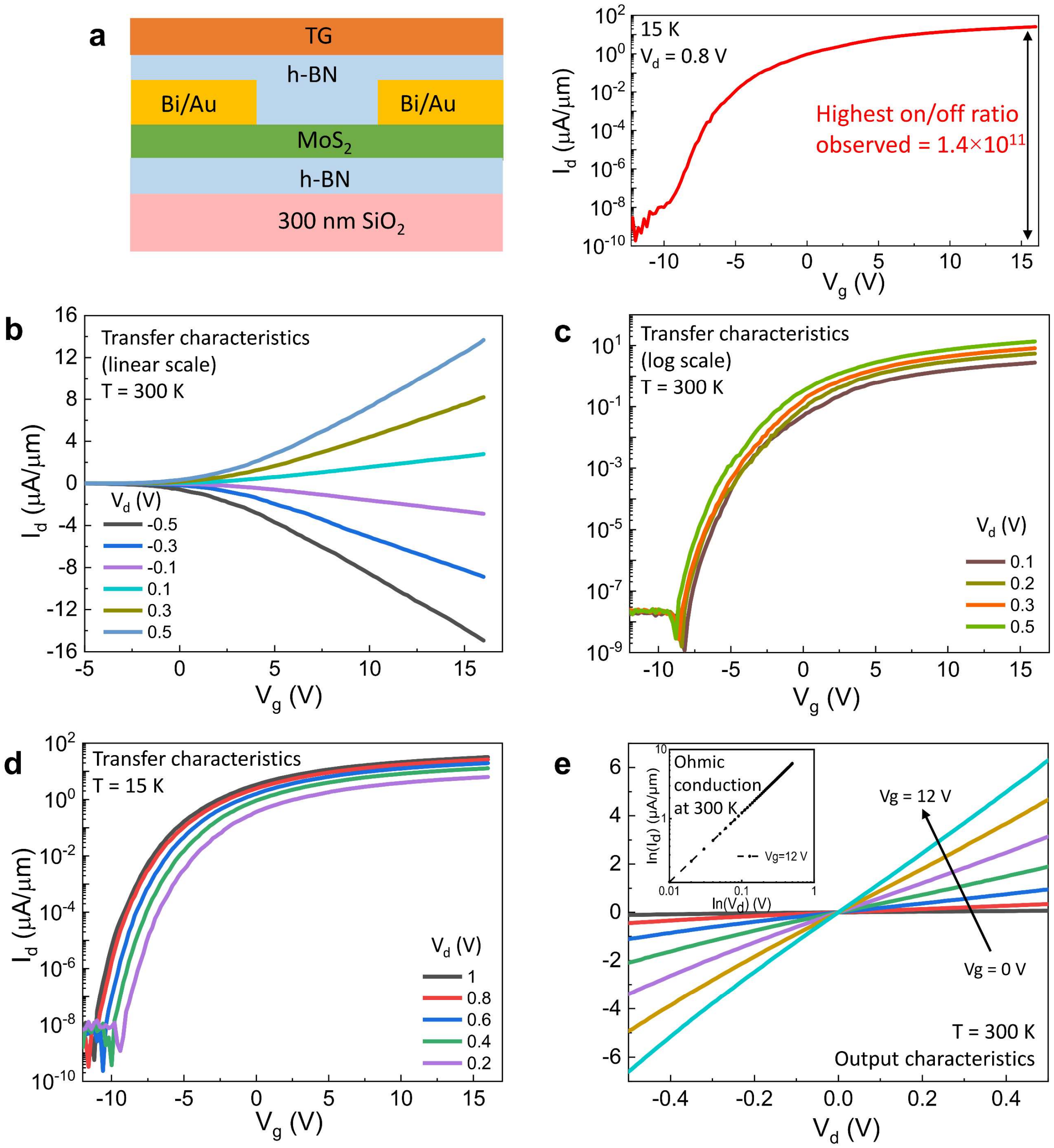

Supplementary Fig. 8 | Electrical performance of the PPC-Bi (Device1: h-BN/MoS_2/h-BN) device. a, Schematic diagram of the MoS_2 FET on the h-BN substrate (h-BN/MoS_2/h-BN) fabricated by the PPC method using Bi contact (PPC-Bi). **b,c,** Transfer characteristics (I_d-V_g) of the device plotted as a function of V_d in linear (**b**) and logarithmic (**c**) scale. **d,** I_d-V_g of the device at low temperature (15 K). **e,** Output characteristics (I_d-V_d) of the device as a function of V_g at 300 K. Inset represents the ln(I_d)-ln(V_d) plot at V_g = 12 V, that exhibits linear behavior demonstrating Ohmic conduction.

Device type: PMMA-Bi (SiO_2/MoS_2/h-BN)

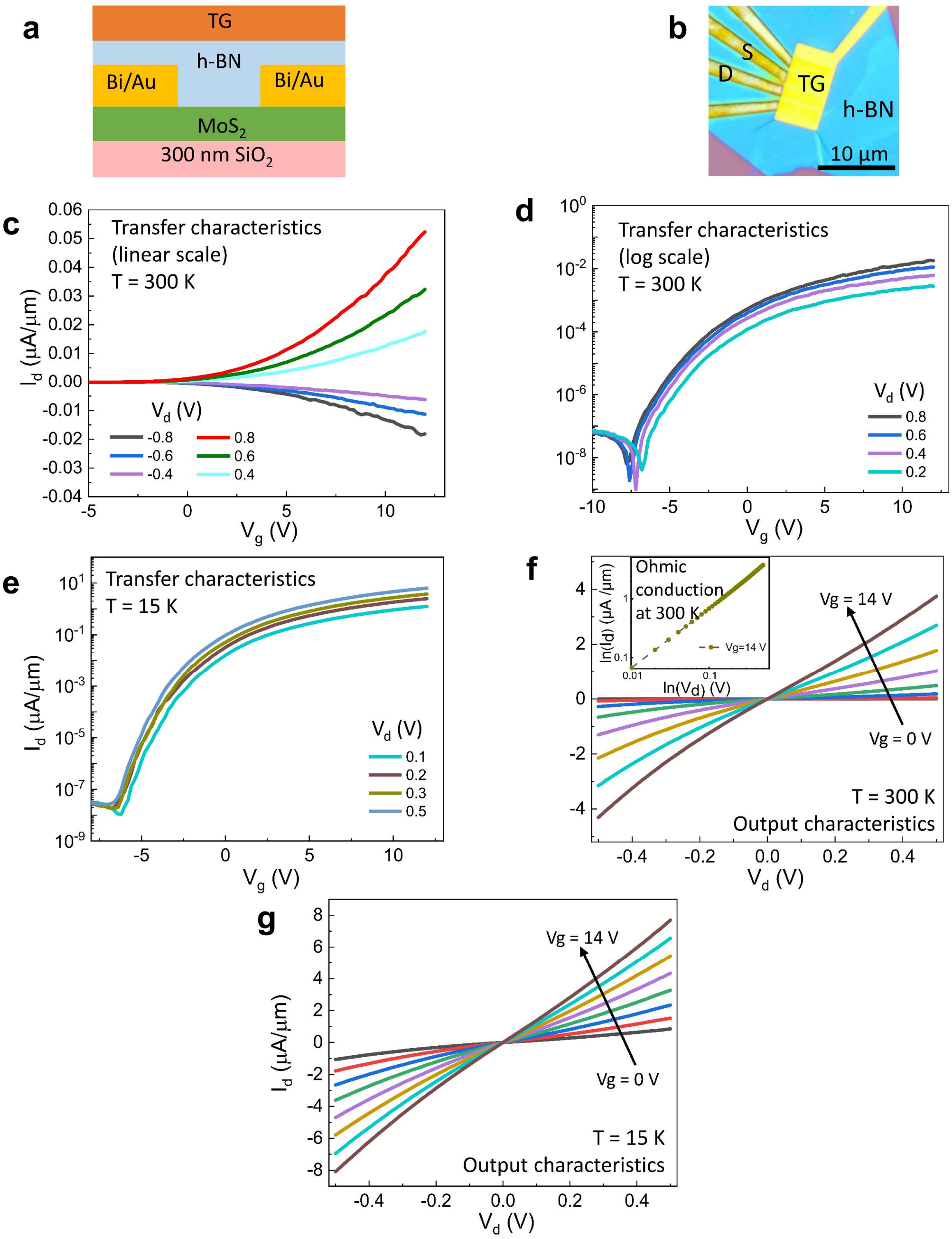

Supplementary Fig. 9 | Electrical performance of the PMMA-Bi (Device4: SiO_2/MoS_2/h-BN) device. **a,b,** Schematic diagram (**a**) and optical micrograph (**b**) of the MoS_2 FET on SiO_2 substrate (SiO_2/MoS_2/h-BN) fabricated by the PMMA method using Bi contact (PMMA-Bi). **c,d,** Transfer characteristics (I_d-V_g) of the device plotted as a function of V_d in linear (**c**) and logarithmic (**d**) scale. **e,** I_d-V_g of the device at low temperature (15 K). **f,** Output characteristics (I_d-V_d) of the device as a function of V_g at 300 K. Inset represents the ln(I_d)-ln(V_d) plot at V_g = 14 V, that exhibits linear behavior demonstrating Ohmic conduction. **g,** I_d-V_d of the device as a function of V_g at low temperature (15 K).

Device type: PPC-Ti (SiO_2/MoS_2/h-BN)

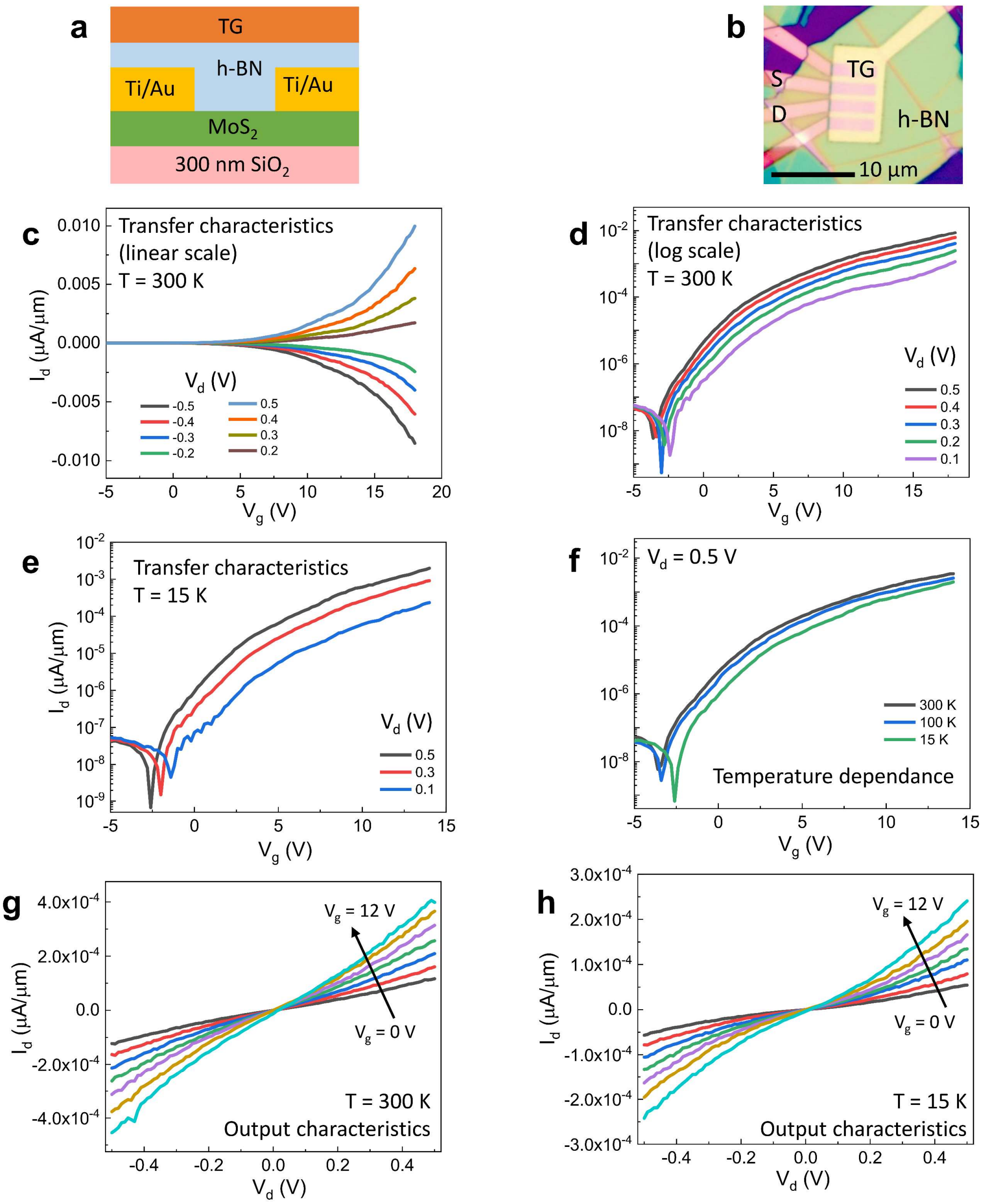

Supplementary Fig. 10 | Electrical performance of the PPC-Ti (Device3: SiO_2/MoS_2/h-BN) device. a,b, Schematic diagram (**a**) and optical micrograph (**b**) of the MoS_2 FET on SiO_2 substrate (SiO_2/MoS_2/h-BN) fabricated by the PPC method using Ti contact (PPC-Ti). **c,d,** Transfer characteristics (I_d-V_g) of the device plotted as a function of V_d in linear (**c**) and logarithmic (**d**) scale. **e,** I_d-V_g of the device at low temperature (15 K). **f,** Temperature-dependent I_d-V_g of the device. **g,h,** Output characteristics (I_d-V_d) of the device as a function of V_g at 300 K (**g**) and 15 K (**h**).

Device type: PMMA-Ti (SiO_2/MoS_2/h-BN)

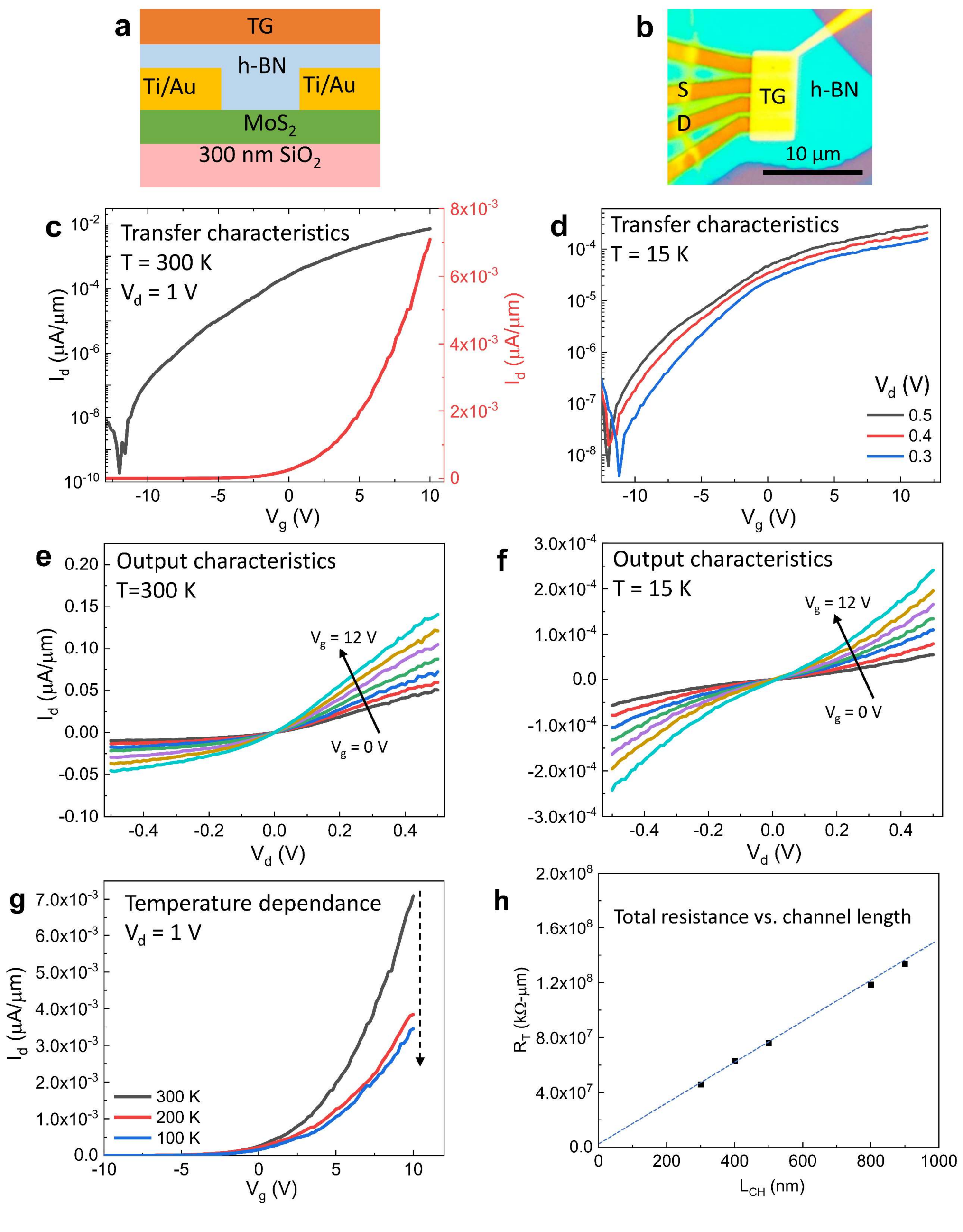

Supplementary Fig. 11 | Electrical performance of the PMMA-Ti (Device5: SiO_2/MoS_2/h-BN) device. **a,b,** Schematic diagram (**a**) and optical micrograph (**b**) of the MoS_2 FET on SiO_2 substrate (SiO_2/MoS_2/h-BN) fabricated by the PMMA method using Ti contact (PMMA-Ti). **c,** Transfer characteristics (I_d-V_g) of the device plotted in log (left, black y-axis) and linear (right, red y-axis). **d,** I_d-V_g of the device at low temperature (15 K). **e,f,** Output characteristics (I_d-V_d) of the device as a function of V_g at 300 K (**e**) and 15 K (**f**). **g,** Temperature-dependent I_d-V_g of the device exhibiting a reduction in I_d with decreasing temperatures. **h,** R_C between Ti and semiconducting MoS_2 extracted using transfer-length method (TLM) for Device5.

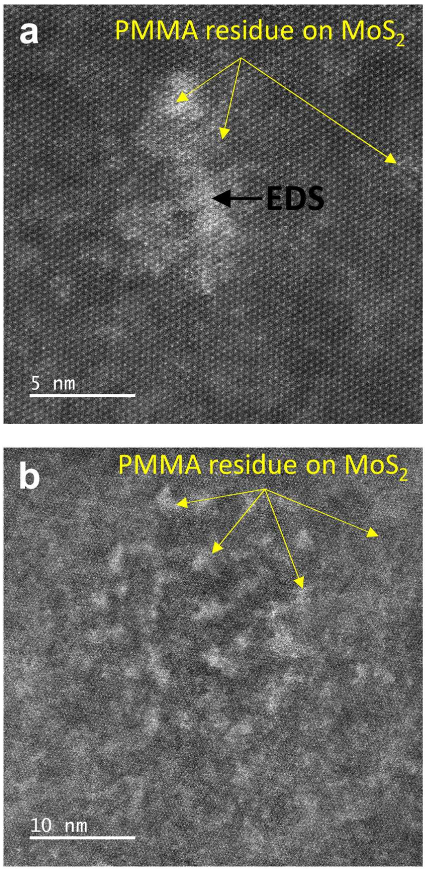

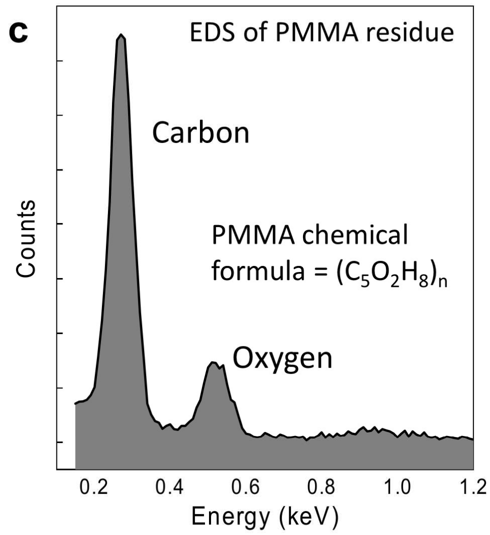

d

Element	Mass%	Atom%
C	91.91	93.80
O	8.08	6.19
Total	100.00	100.00

Supplementary Fig. 12 | TEM analysis of the PMMA residue on the TMD surface. a,b, High-resolution transmission electron microscopy (HR-TEM) images of the visible PMMA residue on the MoS_2 surface. High and low magnifications are shown in Fig. a and b respectively. **c,d,** Energy dispersive spectroscopy (EDS) analysis of the PMMA residue composition (black arrow in a). Carbon and oxygen atoms are present similar to PMMA chemical compounds.

Device type: PPC-Bi (SiO_2/WS_2/h-BN)

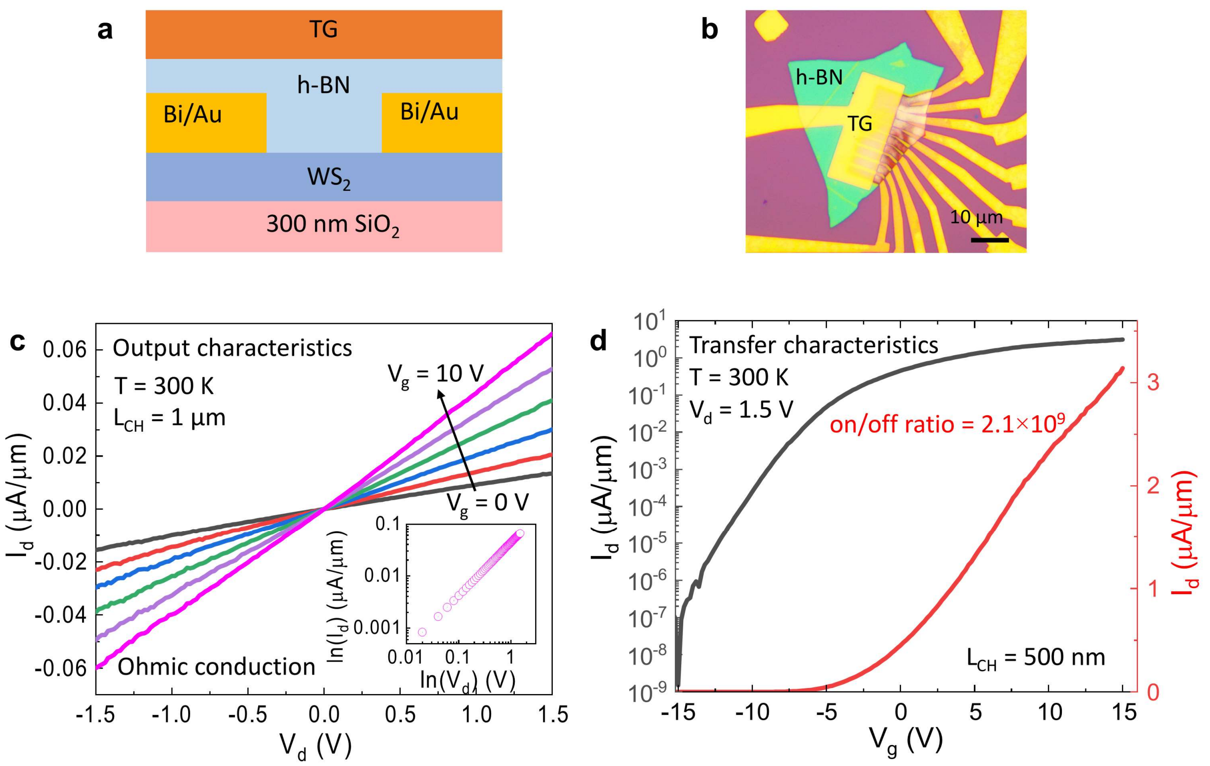

Supplementary Fig. 13 | Electrical performance of the PPC-Bi (SiO_2/WS_2/h-BN) device. a,b, Schematic diagram (**a**) and optical micrograph (**b**) of the WS_2-FET on SiO_2 substrate (SiO_2/WS_2/h-BN) fabricated by the PPC method using Bi contact (PPC-Bi). **c,** Output characteristics (I_d-V_d) of the device as a function of V_g at 300 K. Inset represents the $\ln(I_d)$-$\ln(V_d)$ plot (V_g = 10 V) that exhibits linear behavior demonstrating Ohmic conduction in WS_2-FET. **d,** Transfer characteristics (I_d-V_g) of the device plotted in log (left, black y-axis) and linear (right, red y-axis) scales showing on/off ratio ≈ 2.1×10^9 at 300 K.

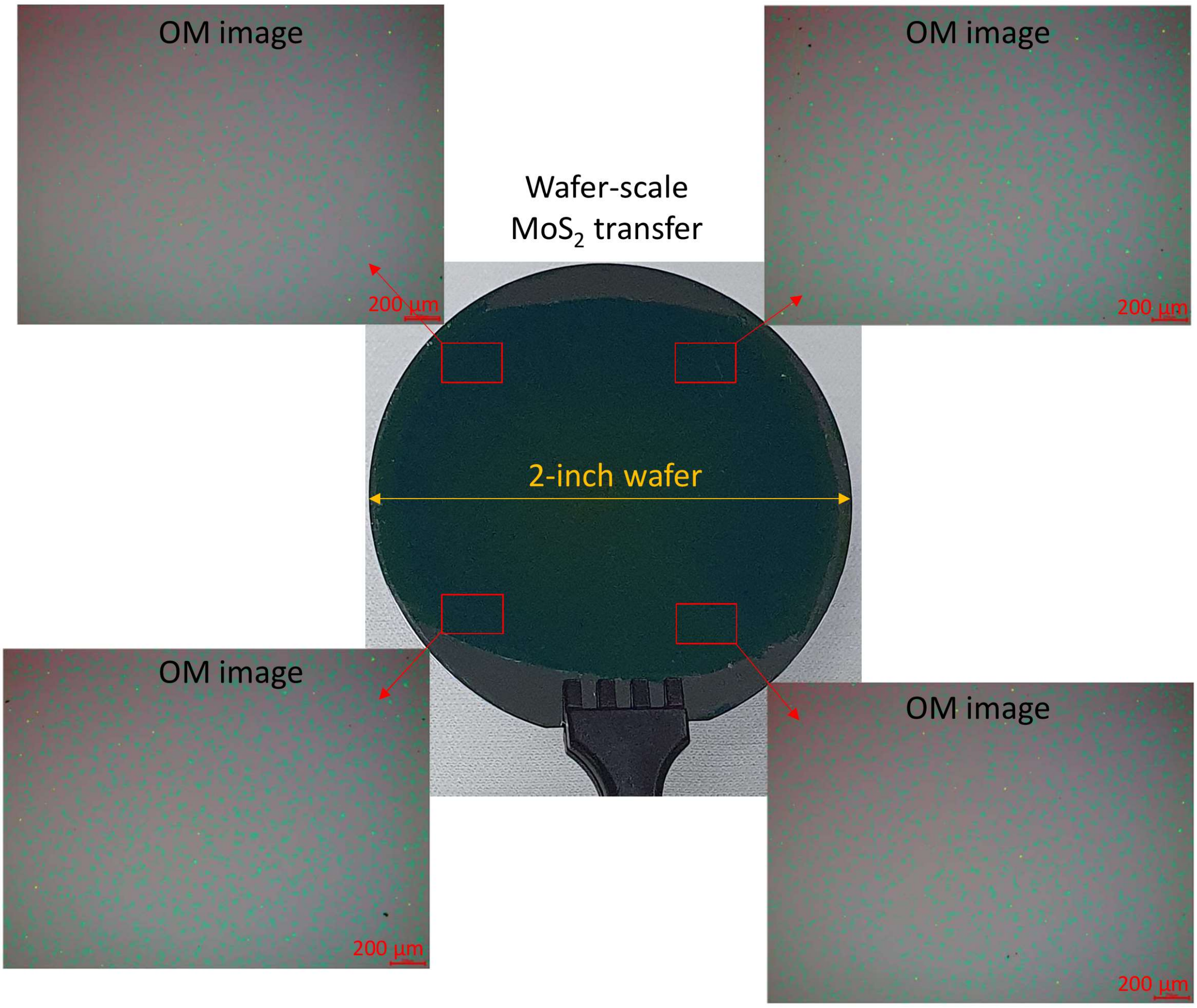

Supplementary Fig. 14 | Wafer-scale MoS_2 film transfer by PPC method. Photograph (middle panel) of the CVD-MoS_2 transferred using the PPC method on a 2-inch Si/SiO_2 wafer. Optical micrograph (OM) images (four corner panels) of the MoS_2 after PPC removal.

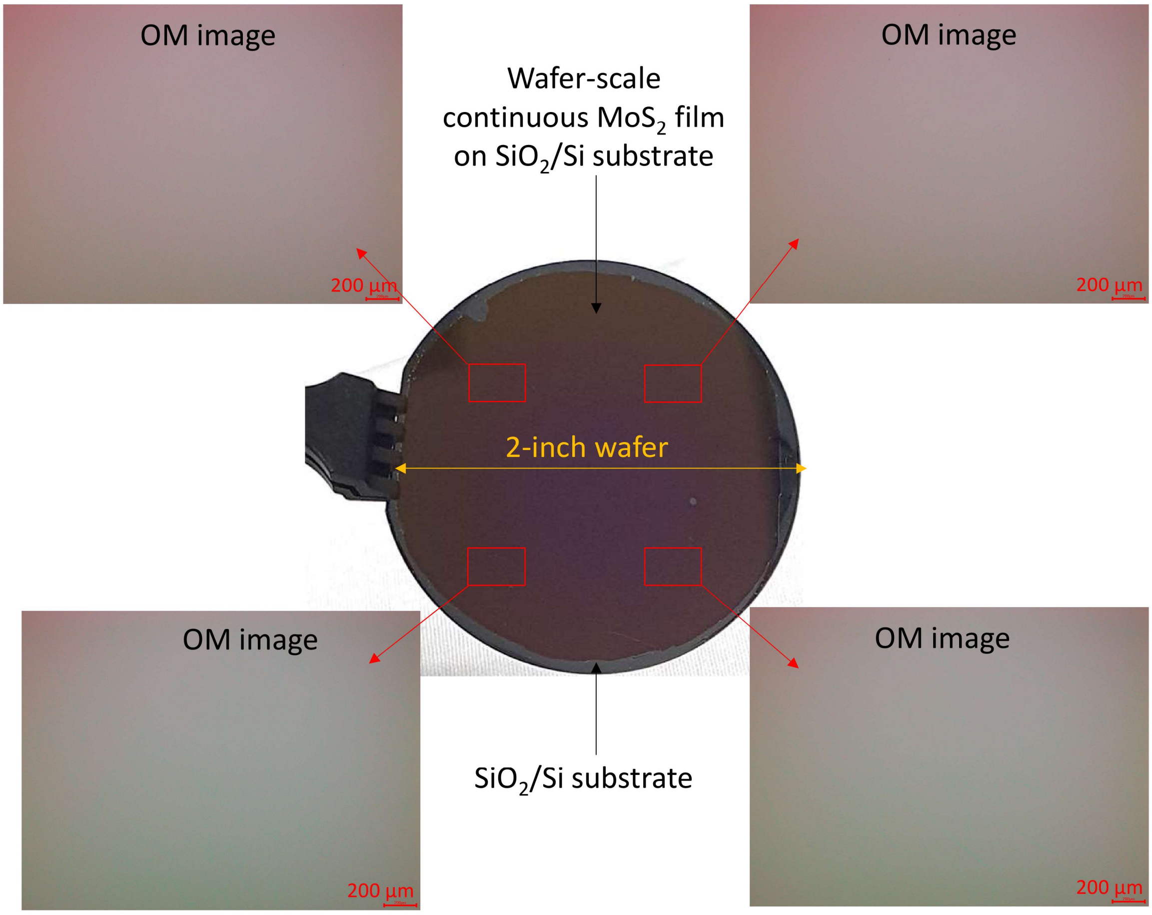

Supplementary Fig. 15 | Wafer-scale continuous MoS_2 film transfer by PPC method. Photograph (middle panel) of the continuous CVD-MoS_2 film transferred using the PPC method on a 2-inch Si/SiO_2 wafer. Optical micrograph (OM) images (four corner panels) of the MoS_2 after PPC removal.

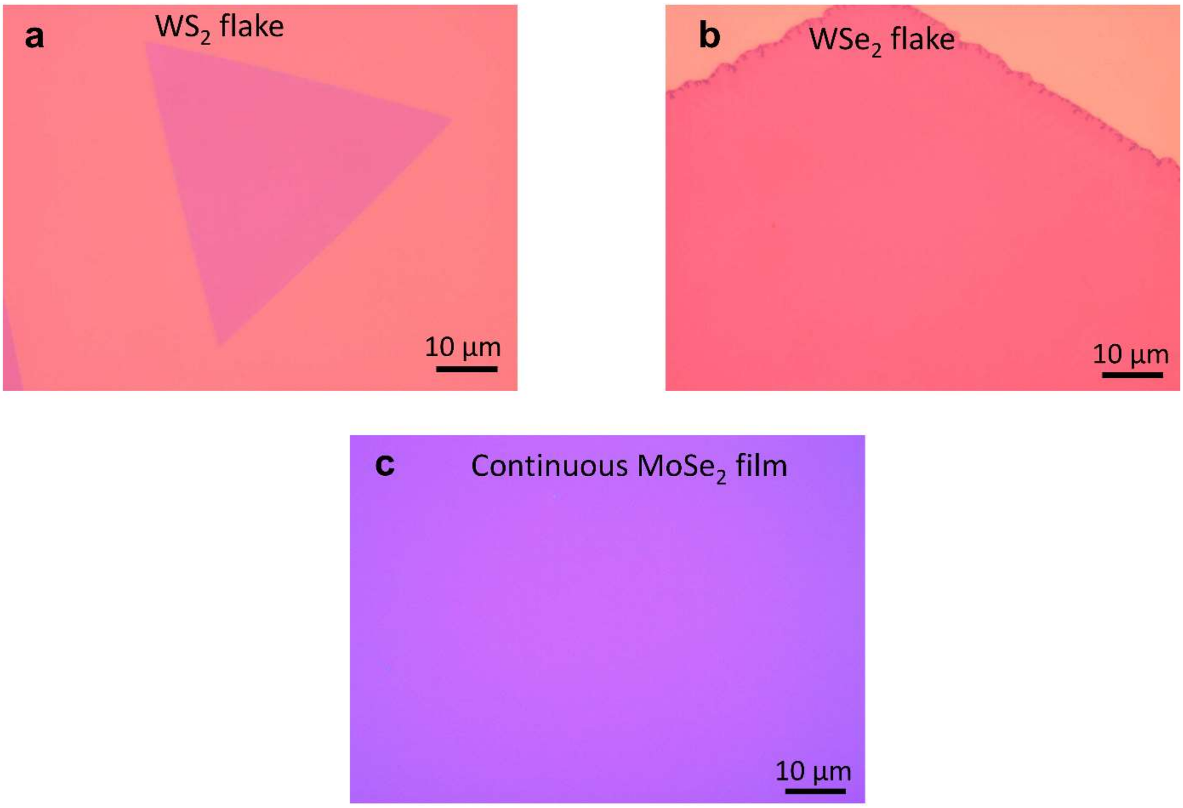

Supplementary Fig. 16 | Optical micrographs of WS_2, WSe_2, and $MoSe_2$ using the PPC-transfer method. a, Optical micrograph of the monolayer WS_2 on SiO_2/Si substrate. **b,** Optical micrograph of the monolayer WSe_2 on a 300 nm thick SiO_2/Si substrate. **c,** Optical micrograph of the wafer-scale continuous $MoSe_2$ film transferred using the PPC method on identical SiO_2/Si substrate. Ultraclean TMDs were observed with negligible PPC residues.

Supplementary Note 1 | Statistical analyses of the residue coverage and contact resistance

Statistical analyses were conducted using the "Standard Error" (SE) calculation method[3] using

$$SE = \frac{\sigma}{\sqrt{n}} \dots\dots\dots\dots\dots\dots\dots\dots\dots (1)$$

Where,
SE = standard error
σ = standard deviation
n = number of measurements

It should be noted that the standard deviation (σ) was given by

$$\sigma = \sqrt{\frac{\sum(x_i - \mu)^2}{n}} \dots\dots\dots\dots\dots\dots\dots\dots\dots\dots (2)$$

Where,
x_i = Value of the measurements
μ = The mean value of the measurements

Using the above we obtain the SE in the residue coverage and contact resistance as shown in the following tables.

Standard error in the contact resistance:

Sample description	Contact resistance (Ω-μm)	Standard error (%)
PPC-Bi (15 K) (Device1: h-BN/MoS_2/h-BN)	78	± 12
PPC-Bi (300 K) (Device1: h-BN/MoS_2/h-BN)	111	± 12.76
PPC-Bi (300 K) (Device2: SiO_2/MoS_2/h-BN)	112	± 8.87

Standard error in the residue coverage:

Sample description	Residue coverage (%)	Standard error (%)
PPC on MoS_2 surface	0.08	± 0.0065
PMMA on MoS_2 surface	35	± 0.0059
PMMA on SiO_2 surface	43	± 0.0061

Supplementary Note 2 | DFT calculation detail:

We performed ab *initio* calculations based on density functional theory (DFT)[4,5] as implemented in the Vienna ab *initio* simulation package (VASP)[6,7] with projector augmented wave potentials[8,9]. The Ceperley-Alder form[10] within the local density approximation (LDA) and Perdew-Burke-Ernzerhof (PBE) form[11] was employed for the exchange-correlation functional with the generalized gradient approximation (GGA) with non-local van der Waals correction such as optB86b[12], rev-vdW-DF2[13]and rvv10[14]. The energy cutoff was set to 500 eV for all calculations. The Brillouin zone was sampled using a 2x2x1 Gamma-centered k-grid. Atomic relaxations were done until the Helmann-Feynman force acting on every atom became smaller than 0.01 eV/Å. We note that DFT approach is challenging to comprehensively account for the complexity of the interactions between the polymers in the experimental setup. This difficulty arises primarily due to the hefty computational cost, with factors like temperature effects and configurational entropy related to the amorphization of polymers playing significant roles. Therefore, we simplified the scenario by simulating the adsorption of a trimer on a MoS_2.

The density of states (DOS) indicates well-localized states for the PMMA trimer when the backbone is close to MoS_2, while hybridization between the PMMA-trimer and MoS_2 occurs when the carbonyl group is close (Supplementary Fig. 17 a, c, d). In the case of PPC, the changes in charge transfer and DOS are not significantly different when comparing the scenarios, where the PPC backbone is close to MoS_2 and on the other hand the PPC carbonyl group is close to MoS_2 (Supplementary Fig. 17 b, e, f). This suggests that stronger adsorption occurs when the PPC backbone is close to MoS_2, primarily due to the difference in van der Waals interactions (~344 meV), compared to the attractive forces resulting from charge transfer.

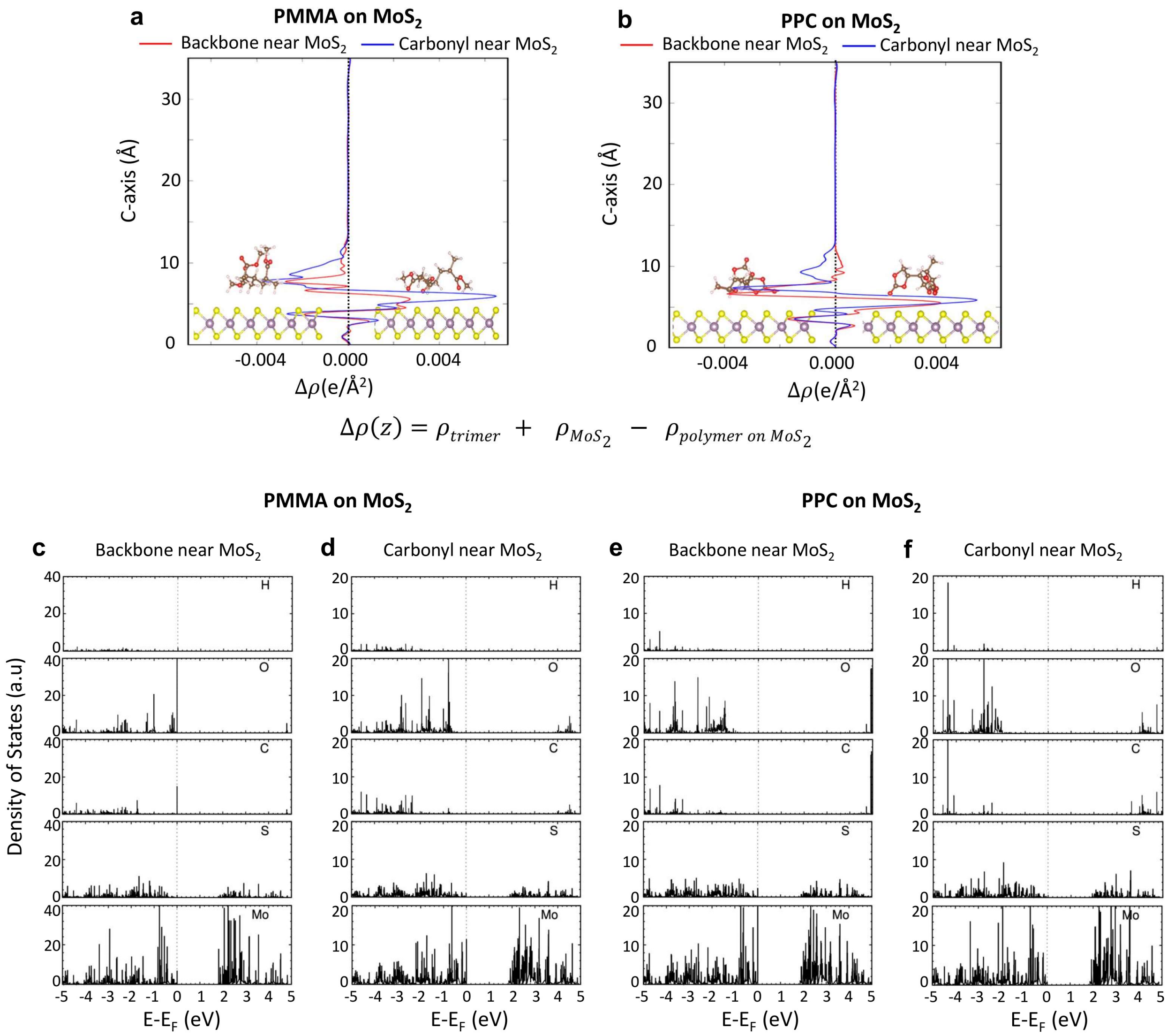

Supplementary Fig. 17 | Charge difference and electronic structure of the monolayer MoS_2 with PMMA and PPC attachments using PBE+vdW (rvv10). a,b, Charge difference of (a) PMMA-backbone and carbonyl, (b) PPC-backbone and carbonyl trimer on MoS_2**. c-f,** the predicted density of states for only trimer when PMMA-backbone (c), carbonyl (d), and PPC-backbone (e), carbonyl (f) trimers are adsorbed on MoS_2.

Supplementary Table 1| Electrical measurements parameters for different device types

Device types	Contact metal	Contact type	R_T (KΩ-µm)	R_c (Ω-µm)	$\mu_{FE, 2t}$ (cm^2/Vs)	I_{ON} (µA/µm) (V_d V)	I_{ON}/I_{OFF}
PPC-Bi (15 K) (Device1: h-BN/MoS_2/h-BN)	Bi	Ohmic	59	78	20	1392 (2.5)	1.4×10^{11}
PPC-Bi (300 K) (Device1: h-BN/MoS_2/h-BN)	Bi	Ohmic	75	111	15	1316 (2.5)	5×10^{9}
PPC-Bi (15 K) (Device2: SiO_2/MoS_2/h-BN)	Bi	Ohmic	38	92	17	1209 (2.5)	7.9×10^{10}
PPC-Bi (300 K) (Device2: SiO_2/MoS_2/h-BN)	Bi	Ohmic	66	112	12	582 (2.5)	7.1×10^{8}
PMMA-Bi (300 K) (Device4: SiO_2/MoS_2/h-BN)	Bi	Ohmic	116	138	0.03	514 (2.5)	1.2×10^{8}
PPC-Ti (300 K) (Device3: SiO_2/MoS_2/h-BN)	Ti	Schottky	11×10^{5}	$\sim 10^{5}$	0.03	0.57 (1)	7.3×10^{6}
PMMA-Ti (300 K) (Device5: SiO_2/MoS_2/h-BN)	Ti	Schottky	20×10^{5}	38×10^{5}	0.007	0.14 (0.5)	4.6×10^{4}

Contact resistances are extracted at a gate voltage $V_g = 12$ V for monolayer MoS_2.

References

1. Wong, C. P. Y., Troadec, C., Wee, A. T. S. & Goh, K. E. J. Gaussian Thermionic Emission Model for Analysis of Schottky-Barrier Devices. *Phys. Rev. Appl.* **14**, 054027 (2020).
2. Yu, W. J. *et al.* Vertically stacked multi-heterostructures of layered materials for logic transistors and complementary inverters. *Nat. Mater.* **12**, 246–252 (2013).
3. Guo, S., Gregory, G., Gabor, A. M., Schoenfeld, W. V. & Davis, K. O. Detailed investigation of TLM contact resistance measurements on crystalline silicon solar cells. *Sol. Energy* **151**, 163–172 (2017).
4. Hohenberg, P. & Kohn, W. Inhomogeneous Electron Gas. *Phys. Rev.* **136**, B864–B871 (1964).
5. Kohn, W. & Sham, L. J. Self-Consistent Equations Including Exchange and Correlation Effects. *Phys. Rev.* **140**, A1133–A1138 (1965).

6. Kresse, G. & Hafner, J. *Ab initio* molecular dynamics for liquid metals. *Phys. Rev. B* **47**, 558–561 (1993).
7. Kresse, G. & Furthmüller, J. Efficient iterative schemes for *ab initio* total-energy calculations using a plane-wave basis set. *Phys. Rev. B* **54**, 11169–11186 (1996).
8. Blöchl, P. E. Projector augmented-wave method. *Phys. Rev. B* **50**, 17953–17979 (1994).
9. Kresse, G. & Joubert, D. From ultrasoft pseudopotentials to the projector augmented-wave method. *Phys. Rev. B* **59**, 1758–1775 (1999).
10. Ceperley, D. M. & Alder, B. J. Ground State of the Electron Gas by a Stochastic Method. *Phys. Rev. Lett.* **45**, 566–569 (1980).
11. Perdew, J. P., Burke, K. & Ernzerhof, M. Generalized Gradient Approximation Made Simple. *Phys. Rev. Lett.* **77**, 3865–3868 (1996).
12. Klimeš, J., Bowler, D. R. & Michaelides, A. Van der Waals density functionals applied to solids. *Phys. Rev. B* **83**, 195131 (2011).
13. Hamada, I. van der Waals density functional made accurate. *Phys. Rev. B* **89**, 121103 (2014).
14. Sabatini, R., Gorni, T. & de Gironcoli, S. Nonlocal van der Waals density functional made simple and efficient. *Phys. Rev. B* **87**, 041108 (2013).